Inorganic Chemistry

pubs.acs.org/IC Article

Structural Stability and Photoluminescence Property of Cs_2UCl_6 Single Crystal Derived from Spent Nuclear Fuel

Yibo Wang, Kun Yang,* Feida Chen, Xianlin Qu,* Yanmei He, Daniu Han, and Xiaobin Tang

Cite This: *Inorg. Chem.* 2025, 64, 3178−3187 Read Online

ACCESS | Metrics & More | Article Recommendations | Supporting Information

ABSTRACT: The recycling and reuse of trace uranium from spent nuclear fuel is of great significance for the safety management of the nuclear fuel cycle. However, stabilization of low-valent uranium has always been a challenge due to the ultraoxidizable nature of uranium ions, which remains relatively uncharted territory in spent fuel treatment. In the current study, U^{4+} was immobilized in Cs_2UCl_6 single crystal with a perovskite structure from uranyl under a strong acidic environment. A comprehensive and detailed understanding of Cs_2UCl_6 at the atomic scale has been achieved by combining density functional theory (DFT) with high-resolution integrated differential phase contrast scanning transmission electron microscopy (iDPC-STEM) imaging, which was captured by utilizing Cs-corrected TEM for the first time. Furthermore, the results obtained from X-ray excitation and the photoexcitation effects produced by PL at 280, 330, and 360 nm provide compelling evidence for the ability of U^{4+} to form excitable bands around the Fermi level. The as-synthesized Cs_2UCl_6 demonstrates excellent thermal stability above 275 °C, as evidenced by in situ Raman spectroscopy and thermogravimetric analysis, while a degradation pathway initiated by CsCl upon exposure to water vapor was revealed by synchrotron X-ray diffraction. Thermal and chemical stability can be further elevated by consolidating it into a metal−organic framework (MOF) via hot pressing. The current study provides a promising strategy to reuse and functionalize the spent nuclear fuel.

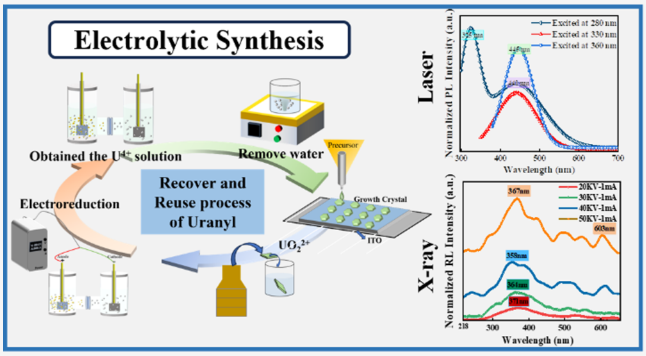

INTRODUCTION

The wide spreading of nuclear energy around the world generates tons of nuclear waste containing transuranic elements, radionuclides, etc., with an overarching goal of either reprocessing or immobilization.[1,2] The plutonium uranium recovery by extraction (PUREX) process is one of the closed fuel cycle methods that have been industrially realized worldwide, which involves the dissolution of fuel rods, separation of metal chips from radioactive elements, and extraction of the spending uranium and plutonium from the organic solvent TBP with an efficiency higher than open fuel cycle.[3,4] However, several radioactive elements, including high-level waste products such as Sr, Cs, Tc, Cl, and I, coexist with a trace amount of uranium and cannot be fully separated or recovered through the PUREX process, which is then immobilized into glass or ceramic waste-form followed by the geological repository.[5] Therefore, it is critical to develop advanced separation materials to recover trace amounts of uranium from the PUREX process, which can reduce the environmental burden of waste immobilization.

Several innovative methods have been proposed for the separation and reuse of uranium, including the use of graphene oxide,[6,7] metal−organic frameworks,[8] organic frameworks,[9,10] and biomass.[11] For instance, uranium can be selectively separated and recovered using a metal−organic framework (MOF) intercalated graphene oxide.[12] Electrostatic interactions between uranyl ions and functional groups in biopolymers have been harnessed to demonstrate uranium recovery efficiencies of up to 73%.[13] The use of inductively coupled optical technology and magnetic biochar materials has been shown to significantly enhance the overall separation and detection efficiency of uranium in wastewater.[14,15]

Instead of merely separating the uranium, the functionalization of the uranyl has garnered continuous attention due to its superior photoelectric properties.[16−19] For instance, mixed-valence uranium clusters, U(V/VI) compounds with a high attenuation coefficient for high-energy photons, exhibit robust semiconductor properties. The device effectively converts X-ray photons directly into electrical signals.[20] UO_2^{2+} exhibits excellent luminescence when excited by X-ray photoluminescence, making it a promising U-based scintillator.[21−23] Compounds based on U^{4+}, such as UTe_2, possess heavy

Received: September 25, 2024
Revised: February 1, 2025
Accepted: February 5, 2025
Published: February 12, 2025

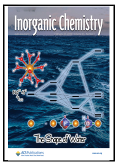

https://doi.org/10.1021/acs.inorgchem.4c04076
Inorg. Chem. 2025, 64, 3178−3187

Fermion triplets, representing a class of high-performance superconducting materials.[24−26] Therefore, it is of immense significance to utilize separation technology combined with its functional properties to transform the spent fuel into a "treasure" and realize the efficient use of U, enabling it to have potential applications in special scenarios.

Recently, matrixes such as double perovskite with a crystalline structure of A_2BX_6, which allows the simultaneous separation and immobilization of the residual uranium after the PUREX process, have gradually become one of the promising materials for the separation and immobilization of high-level nuclear waste.[27−29] Researchers have identified that harnessing the multifaceted sites within the perovskite structure can immobilize a diverse array of nuclides, making it particularly effective for elements that act as heat sources, such as Cs/Sr.[30] Both $Cs_3Bi_2I_9$ and Cs_2SnCl_6 perovskite have achieved a waste loading as high as 50 and 38 wt % for Cs and Cl, respectively, based on our previous research.[31] However, the possibility of incorporating transuranic actinides, i.e., uranium or so, into the perovskite matrix remained an open question, especially under a highly acidic environment. The B-site elemental substitution of Sn with U leads to the formation of Cs_2UCl_6 with a stable double perovskite structure, which has already been predicted by the Gold−Schmidt tolerance factor.[32] Previous reports proved the viable option for uranium reduction,[33,34] and can occupy lattice positions as a doping element.[35] Unfortunately, the valence state of the uranium was not fully understood, while the functionalization of the uranyl was further limited by the synthesis of high-quality single crystal. Therefore, the viability of synthesizing such a structure from an aqueous phase, particularly under highly acidic conditions with high recovery efficiency, is yet to be determined. The persistence of two uranium oxidation states (U(IV/V)) of U^{6+} reduction during electrolytic reduction poses a challenge in practical spent fuel treatment programs that need to be further revealed. A special configuration of Cs_2UCl_6 with remarkable parallels was observed during the synthesis of the two-dimensional Cs_2SnCl_6 perovskites implying a similar photon property.[36] Furthermore, the underlying mechanism that dominates photon application must be further revealed.

In the current study, the transition of uranyl to double perovskite crystal (Cs_2UCl_6) subjected to a highly acidic environment was carried out based on a one-step electrolytic reduction strategy with a conversion efficiency of about 70%, with both Cs and U were successfully incorporated into the perovskite matrix to simulate the PUREX process. The synthesis of several single crystals, ranging in scale from tens of micrometers to several millimeters, was completed. Subsequent microstructure was conducted using scanning transmission electron microscopy (STEM). The optical properties of Cs_2UCl_6 were further studied by density functional theory (DFT) and steady-state spectra. The results show that Cs_2UCl_6 exhibits favorable photon responses to UV photons (280, 330, 360 nm) and X-ray, elucidating radioactive transition processes induced by photon excitation, suggesting potential applications for U^{4+} as a functional material in UV absorption and X-ray detection. The current study, anchored in the context of spent fuel treatment, amalgamates theoretical and experimental methodologies to articulate a competent and feasible approach for the post-treatment and functionalization of uranium-depleted materials. The detailed characterization and construction of theoretical models serve as both reference points and sources of insight, contributing to the subsequent advancement of Cs_2UCl_6.

■ EXPERIMENT METHOD

Synthesis of Materials. Uranyl nitrate (UO_2^{2+}) served as the source of U^{6+} in the PUREX process, which came across the electrochemical reduction under an argon atmosphere with a self-assembled electrolytic cell (Figure S1). Uranyl nitrate (80 mg in a 5 mL solvent) was fully dispersed and dissolved in a solvent composed of a mixture of concentrated hydrochloric acid and distilled water with a ratio of 1:70. The anode solution was composed of uranium hexafluoride nitrate, while the corresponding cathode solution was consisted of 5 mL pure solvent. The voltage and current were set as 5 V and current 0.6 mA with pH measured as 0.837. A semipermeable membrane was applied to selectively facilitate the reduction of U^{6+} to a stable U^{4+} state. The total reaction time was set below 12 h to prevent over-reduction. The concentration of U^{6+} significantly decreased after a 10 h electrolysis reaction, as evidenced by in situ Raman (Figure S1). Meanwhile, the cathode solution underwent a noticeable color change from transparent to blue-green, while the anode solution shifted from light-green to nearly transparent. The solution was then stirred and mixed meticulously, followed by curing at 30 °C for 2 h after adding CsCl. Distillation was then performed at temperatures not exceeding 70 °C until complete solution evaporation, leaving light-green Cs_2UCl_6 crystal samples. **Caution!** Uranyl contains the radiational element U-238 that a trained person must handle. Particular attention should be paid to protecting the environment from corrosion caused by acid on human skin during the experiment. In addition to moisture, protection against devices and respiratory corrosion caused by chlorine gas produced during the distillation process is also required.

ZIF-62 and Cs_2UCl_6 composites were consolidated by low temperature (90 °C) and high pressure (350 MPa) hot-pressing with a thermal holding time of 20 min. The entire process was conducted under an argon atmosphere until it completely cooled to room temperature. The sample pellets were then subjected to water corrosion for 72 h under room temperature, followed by drying on their surfaces and a PL spectra test.

Characterization Details. These detailed descriptions of the characterization equipment are summarized in Table S1.

Single Crystal X-ray Diffraction. The system utilized a copper anode X-ray tube (Cu Kα radiation, λ = 1.5406 Å) operated at a voltage of 40 kV and a current of 40 mA. Diffraction patterns were recorded over a 2θ range from 10 to 70° with a step size of 0.02° and a scanning speed of 1° per minute.

Scanning Electron Microscopy. All samples were prepared by dropwise addition to the conductive glass after removal from the precursor solution and rapidly scraped onto the glass to disperse uniformly and achieve growth per unit area to form single crystals. Imaging was performed at an accelerating voltage of 5 kV, providing high-resolution images of the sample surfaces.

Scanning Transmission Electron Microscopy. Transmission electron microscopy (TEM) investigations were operated at an accelerating voltage of 200 kV. High-resolution TEM (HRTEM) images and selected area electron diffraction (SAED) patterns were obtained to analyze the crystalline

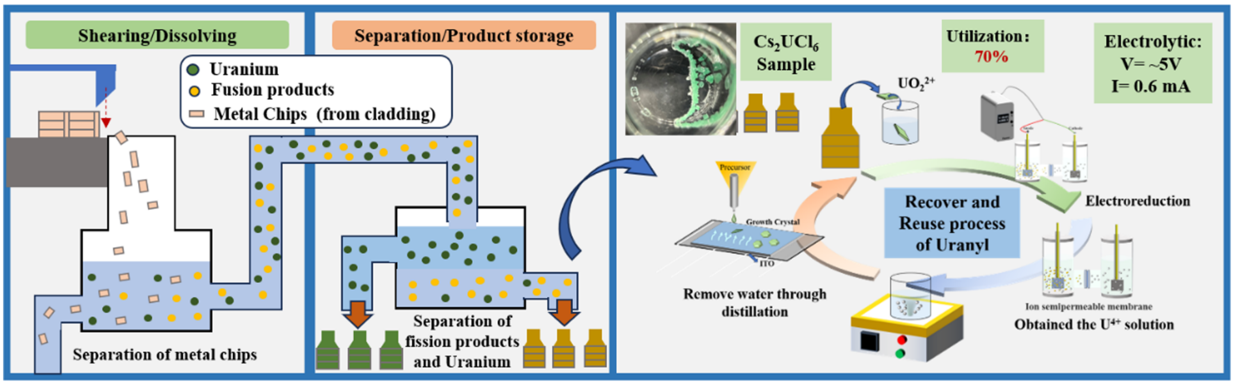

Figure 1. Schematic diagram of the process for preparing Cs_2UCl_6 crystal based on the PUREX process, the inset image is the Cs_2UCl_6 crystal sample.

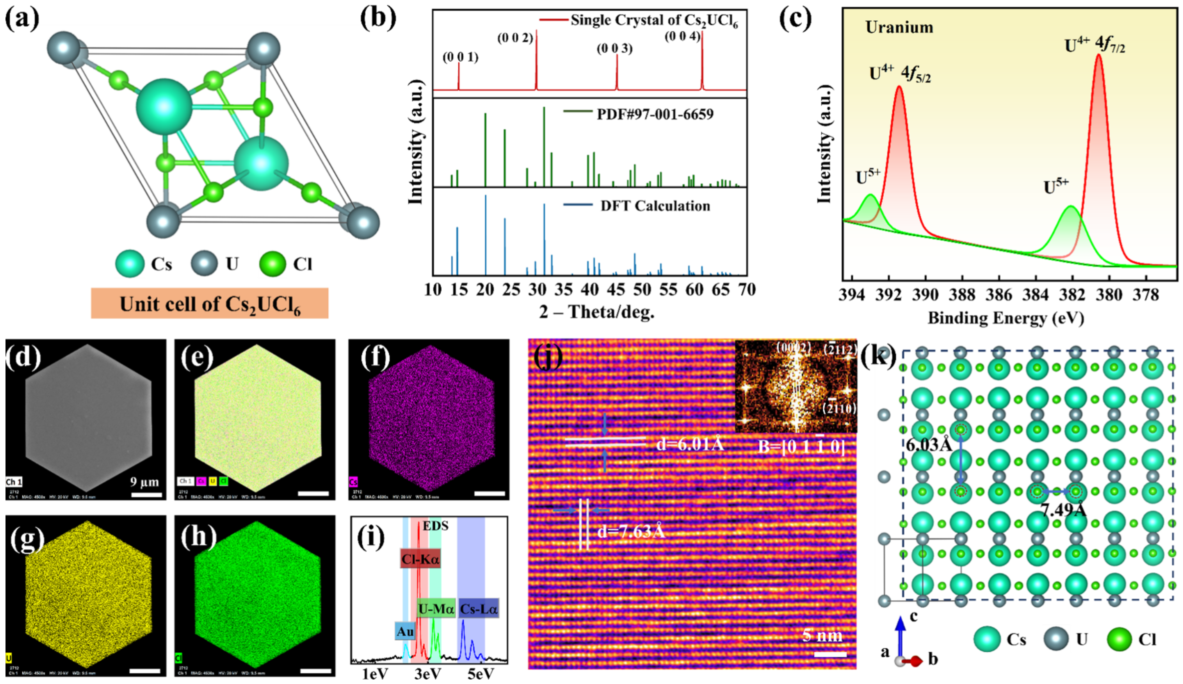

Figure 2. (a) Minimal unit cell of Cs_2UCl_6 crystal. (b) XRD of Cs_2UCl_6 in experiment and DFT calculations. (c) Valence characterized by X-ray photoelectron spectroscopy of the U atom, (d) SEM image with selected one Cs_2UCl_6 single crystal. (e–h) EDS of Cs, U, and Cl in SEM, which are represented in pink, yellow, and green. (i) Energy spectrum of Cs_2UCl_6 single crystal from EDS. (j) Diffraction pattern and microscopic atomic image of Cs_2UCl_6 from HAADF. (k) Lattice plane (1 2 0) of Cs_2UCl_6 from the direction of the front view.

structure of the samples. The TEM samples were prepared by using a focused-ion beam (FIB).

Raman Spectroscopy. The excitation source was a 532 nm laser with a power setting of 1 mW to minimize the sample heating and damage. A 50× objective lens was used for focusing the laser on the sample, and the spectral resolution was set to 1 cm^{-1}. Raman spectra were acquired over a temperature range from −100 to 330 °C. The temperature was controlled with an accuracy of ±0.2 °C. Each spectrum was acquired with an integration time of 10 s, and the measurements were conducted in an inert gas atmosphere to prevent any sample degradation.

Thermogravimetric Analysis (TGA). The samples were heated from room temperature to 500 °C at a heating rate of 10 °C/min under a nitrogen atmosphere at a flow rate of 60 mL/min flow rate. The experiment commenced with a 5 min hold period after the temperature reached 50 °C. The mass loss and thermal stability were recorded and analyzed to understand the decomposition behavior of the materials.

X-ray Photoelectron Spectroscopy (XPS). The system utilized a monochromatic Al Kα X-ray source (1486.6 eV). The spectra were recorded with a pass energy of 20 eV for high-resolution scans and 160 eV for survey scans. The binding energies were calibrated by using the C 1s peak at 284.8 eV as a reference.

UV–Vis Absorption Spectroscopy. The measurements were performed in the 200–400 nm wavelength range. Samples were prepared by loading multiple single crystals of the material into a transparent, solid quartz cuvette with a length of 1 cm. The spectral resolution was set to 1 nm.

Photoluminescence (PL) Spectroscopy. The samples were excited with 280, 330, and 360 nm continuous-wave laser, and the emission was collected over a wavelength range of 380–650 nm. The excitation power was set to 1 mW, and the spectral resolution was 0.5 nm.

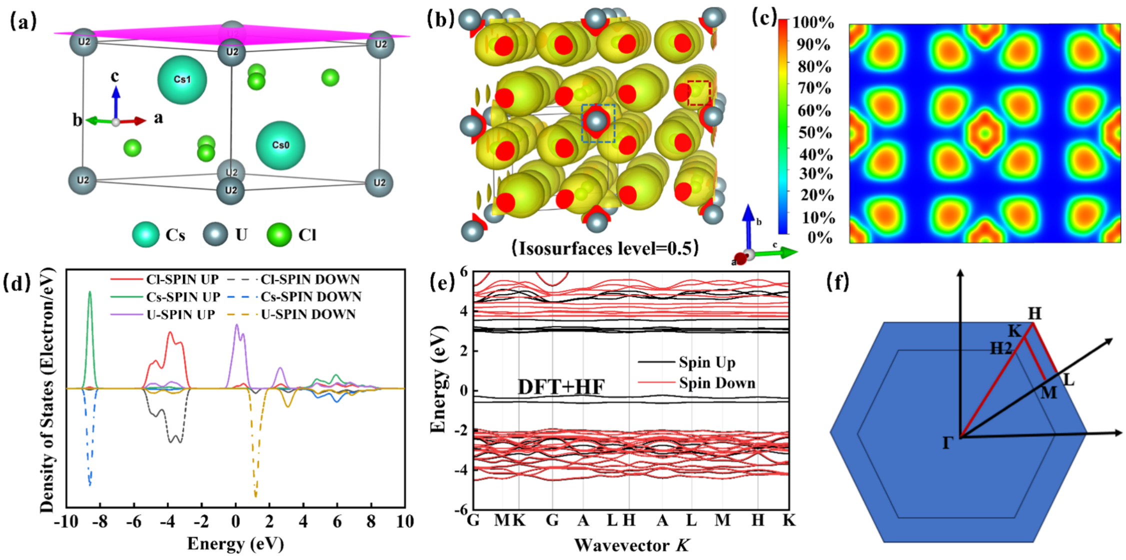

Figure 3. (a) Electronic structure of Cs_2UCl_6 for DFT calculations, the pink area marks the (0 0 1) lattice plane. (b) 3D electron localization function (ELF) of Cs_2UCl_6, the blue dashed line represents the local distribution of U atom electrons, and the red dotted line represents the local distribution of Cl atom electrons, the yellow sphere represents the distribution of electrons in space. (c) 2D ELF of the (1 −1 0) lattice plane, which is the longitudinal section containing U based on 3D ELF. (d) Projected density of states of Cs_2UCl_6. (e) Band structure of Cs_2UCl_6 by HSE with a (f) highly symmetric path in band structure calculations.

Synchrotron. The sensor material used in this characterization was silicon. The energy of the X-ray was 18 keV. The detector module employed Pilatus 2 M. The samples used in the experiment were tested after grinding them into powder. The experiment process was finished at the Shanghai synchrotron radiation facility.

Computation Details. The calculations of Cs_2UCl_6 properties are based on the DFT, which was implemented via Vienna ab initio simulation package (VASP 6.3.0) codes.[37,38] The projector augmented wave (PAW) pseudopotential in reciprocal space by the generalized gradient approximation (GGA) with the Perdew−Burke−Emzerhof (PBE) functional for exchange correlation was used in calculations. All of the parameters in calculations were selected by the minimum energies in structure optimization with spin−orbit coupling (SOC), which is shown in Figure S3. Plane waves with energies reaching 600 eV were employed to describe the electronic wave functions, and the Monkhorst−Pack grid of *k*-points was set as 2 × 2 × 1 for geometries optimization. The force converged above 0.01 eV/Å. Hubbard *U* correction was employed to uranium *f* states calculations with van der Waals (DFT-D3 with Grimme), where the $U-J$ value was set to 0.5 eV. The convergence test of $U-J$ value and lattice constants change was concluded in Figure S4 and Table S2 respectively. The processing of band structure and density of states utilizes the VASPKIT code.[39]

■ RESULTS AND DISCUSSION

Cs_2UCl_6 crystals were synthesized from an aqueous phase in an acid environment. The whole process was tight with the PUREX process, as depicted in Figure 1. The dynamic process of crystal growth during distillation is visually presented in Movie 1 in the Supporting Information. The growth of the Cs_2UCl_6 single crystal contradicts the temperature from 47 to 67 °C because more nucleation sites are formed at higher temperatures to the detriment of crystal growth, with the largest single crystal of approximately 3 mm formed at 47 °C as shown in Figure S1. The Cs_2UCl_6 yielding ratio was further determined as high as 70% in this experiment.

Figure 2a displays the minimal unit cell belonging to the hexagonal system of Cs_2UCl_6 with space group $P\bar{3}m1$. The lattice constants are $a = b = 7.492$, $c = 6.039$, while the lattice angles are $\alpha = 90°$, $\beta = 90°$, and $\gamma = 120°$. Figure 2b shows that X-ray diffraction pattern (XRD) peaks come from the same lattice orientation, (0 0 1), (0 0 2), (0 0 3), and (0 0 4) respectively. The results indicated that the synthesized sample is a high-purity single crystal, which matches well with the standard Cs_2UCl_6 (PDF#97-001-6659). Moreover, the XRD diffraction peaks derived from the structure model refined through DFT calculations are in exact alignment with the experimental XRD pattern of the Cs_2UCl_6 crystals, indicating that the as-synthesized crystals possess a high degree of crystalline purity. The optimized $CsCl:UO_2^{2+}$ ratio of 1.4:1 can be seen for the yielding of high purity Cs_2UCl_6 crystal, with undemanded CsCl can be identified by increasing the $CsCl:UO_2^{2+}$ ratio to 2:1 as denoted by the XRD profile as shown in Figure S5, which can be attributed to the incomplete electrolytic reduction of U^{6+} during the electroreduction process, further suggesting that the synthesis of Cs_2UCl_6 requires access to positively charged tetravalent uranium ions in the sample. The XPS results exhibit a double peak of a $5f^1$ final state containing $5f_{5/2}$ and $5f_{7/2}$ as shown in Figure 2c, which is the typical characterization for U, and the binding energies belonging to 380.5 and 391.3 eV.[20,40] However, a fraction of U^{5+} was rapidly oxidized, which is evidenced by the presence of the O-1s in Figure S6. Also, the morphology features showed the amorphous structure covered on the surface (Figure S7), which can accommodate small molecules such as oxygen and water, in contrast to the step wave structure of Cs_2UCl_6 crystal thus leading to the oxidation of U^{4+}.[41]

The microstructure of Cs_2UCl_6 possesses a near-perfect symmetric hexagonal octahedral can be seen in Figure 2d, with a thickness of approximately 16.96 μm and an average side length of 21.68 μm (Figure S8). A mutually perpendicular

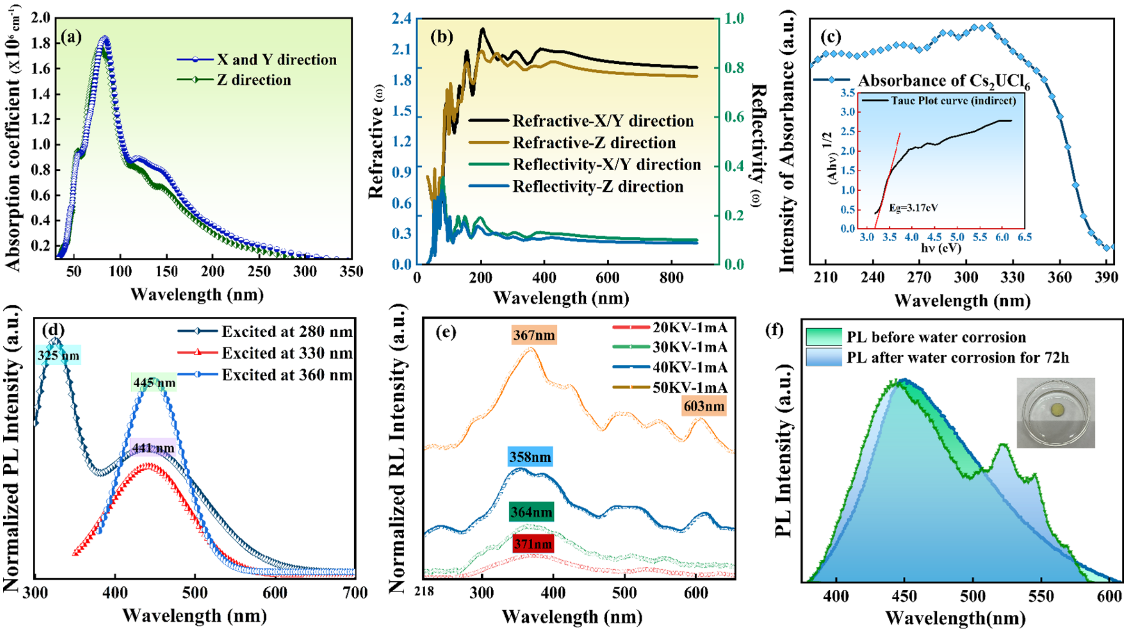

Figure 4. (a) Absorption coefficient of Cs_2UCl_6 from the DFT calculations. Blue represents the absorption coefficient from the X and Y axis. Green represents the absorption coefficient from the Z axis. (b) Secondary frames represent the refractive index and reflectance of Cs_2UCl_6 in different crystalline orientations. (c) UV absorbance curves and optical band gap fits of Cs_2UCl_6. (d) Emission spectra of Cs_2UCl_6 under different wavelength excitation light. (e) Emission spectra of Cs_2UCl_6 at different energies of X-rays. (f) Photoluminescence of composite pellet (ZIF-62 and Cs_2UCl_6) before and after water corrosion; the inset shows the water corrosion of composite pellet.

colattice structure forms in a two-dimensional space, in which growth orientation is mainly perpendicular with (0 0 1) direction during crystal growth.[42] Energy dispersive X-ray spectroscopy (EDS) characterization of the selected Cs_2UCl_6 crystal shows a uniform distribution of the three elements within the single crystal domain with the elemental composition adhering closely to the stoichiometry of Cs_2UCl_6, as shown in Figure 2e−h and Table S3. Combined with the exactly corresponding spectral peaks of Cs, U, and Cl in the energy spectrum of a single crystal in Figure 2i, the results provide further evidence that the composition of Cs_2UCl_6 consists exclusively of these three elements without any excess.

Atomic scale microstructure analysis was carried out based on the integrated differential phase contrast scanning transmission electron microscopy technique (iDPC-STEM) under ultralow electron dose conditions because of the electron-beam sensitive nature of Cs_2UCl_6. The FIB sampling lamella and EDS elemental mappings of Cs_2UCl_6 are depicted in Figure S9. The atomic-resolution iDPC-STEM image confirms the presence of a hexagonal crystalline structure in Cs_2UCl_6, devoid of any crystal defects (Figure 2j). The crystal orientation index of the white line region was identified as [0 1−1 0] by comparing its fast Fourier transform (FFT) in the inset with a standard pattern. The two determined diffraction angles θ_1 and θ_2 are 57.2°and 32.8°as denoted in the atomic-resolution STEM image. Figure 2k illustrates the atomic structure diagram of Cs_2UCl_6, with the position of the (1 2 0) plane in STEM marked. A comparison with the (0 0 1) plane in Cs_2UCl_6 reveals that the two lattice planes are mutually perpendicular, which suggests that the hexagonal crystal morphology data obtained in the SEM (Figure 2d) originates from the (0 0 1) crystal plane, in agreement with previous findings. The results further indicate that the main growth of Cs_2UCl_6 extends along the direction of the a/b axis, which is perpendicular to the [0 0 0 1] crystallographic orientation. A comparison of the interplanar spacing obtained in the atomic structure was 6.03 Å, with the results obtained via STEM 6.01 Å revealing a high degree of agreement between the theoretical and experimental results, thereby substantiating the high quality of the synthesized crystals.

Figure 3a illustrates the electronic structure of Cs_2UCl_6. Cs, U, and Cl occupy the Wyckoff positions 2d, 1a, and 6i, respectively. The three-dimensional electron cloud distribution of Cs_2UCl_6 is presented based on the electron localization function (ELF) in Figure 3b. The results show that Cl atoms predominantly capture electrons, resulting in a more pronounced electron occupancy around the atomic nucleus. In contrast, Cs atoms capture fewer electrons, with a smaller spatial occupancy. The electron projection map of (1−1 1), as depicted in Figure 3c, where U atoms are located, shows that the outer layer electrons exhibit a conical distribution due to substantial electron transfer between U and Cl, leading to spatial distortion after experiencing significant force. Although the U atoms exhibit strong localization characteristics, the bonding properties reveal typical ionic bonding of Cs_2UCl_6. In addition, the results show that the Fermi levels constituting both spin-up and spin-down states arise primarily from orbital hybridization between U and Cl atoms. The density of states (DOS) calculations in Figure 3d indicate that the energy levels at the CBM mainly come from U and Cs atoms, which suggests that the bonding in Cs_2UCl_6 crystals is slightly different from Pb−X (X = Cl, Br, I) based perovskites. Furthermore, the band structure of Cs_2UCl_6 was calculated using the Hybrid Exchange−Correlation Functional (HSE06), as shown in Figure 3e.[43] The results indicate that a more accurate gap value of Cs_2UCl_6 is around 3.14 eV based on a clear high symmetry computational path in Figure 3f.[44] The band structure suggests the presence of a broad indirect band gap, exhibiting similarities to the energy band structure

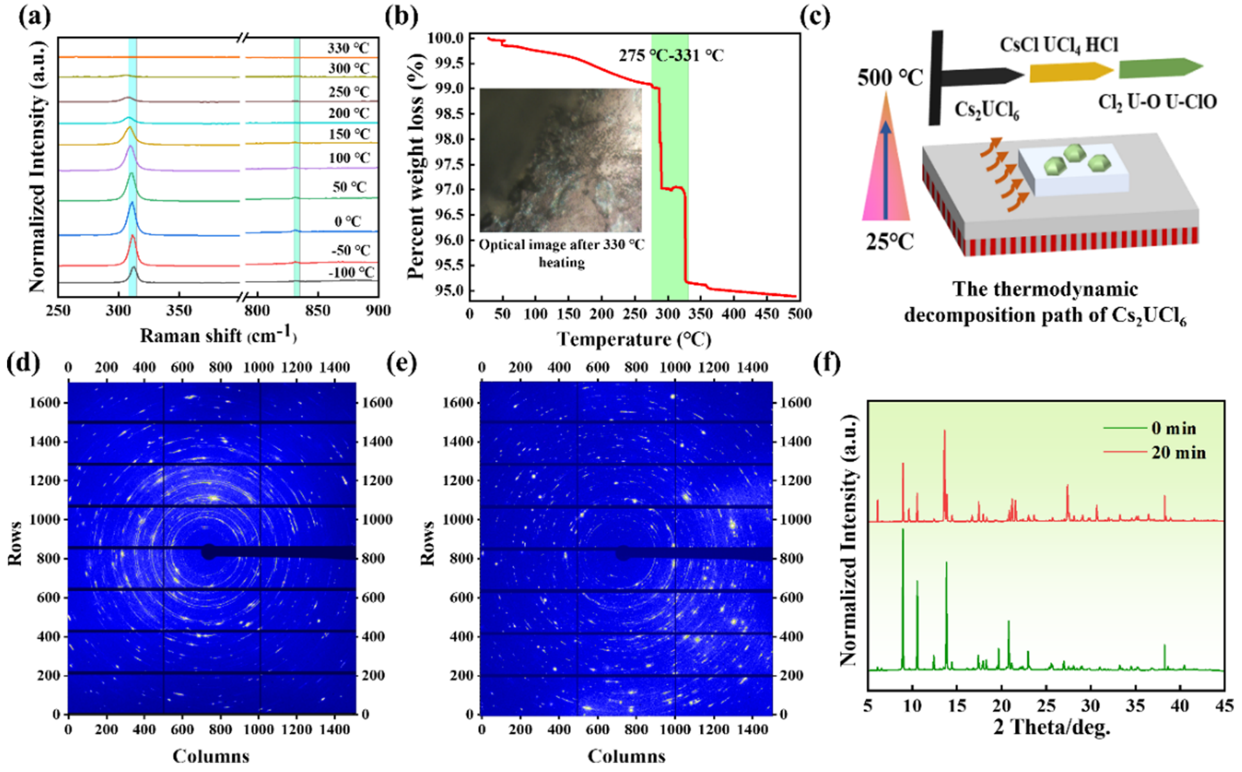

Figure 5. (a) In situ Raman spectra of Cs_2UCl_6 crystals (at 50 °C temperature intervals). (b) Thermal weight loss curve of Cs_2UCl_6 and optical microscopy images at 330 °C. (c) Schematic diagram of the dissociation path of Cs_2UCl_6, (d) two-dimensional (2D) SXRD of Cs_2UCl_6 powder upon the flow of vapor at 0 and (e) 20 min. (f) Typical integrated curves of X-ray patterns at 0 and 20 min.

observed in perovskite. Based on its structural features, we hypothesize the existence of excitation-relaxation for optical properties.

As shown in Figure 4a, the Cs_2UCl_6 shows a wide range of absorption coefficients from 50 to 310 nm with the main peak at 82 nm, which is derived from the HSE06 method. The absorption coefficient value of the Z-axis decreases compared to that of the X/Y axis after 82 nm due to the anisotropic characteristic, which induces a decaying trend of the dielectric function. The calculation method can be seen in eq S3 (Supporting Information). Similarly, this attenuation results in a reduction in the refractive index and reflectivity in the Z-axis direction as shown in Figure 4b. The steady-state absorption of Cs_2UCl_6 is located between 200 and 315 nm, with a slight attenuation of 75.21% beyond 315 nm (Figure 4c). The optical band gap value of 3.17 eV was obtained using the indirect fitting method from the Tauc plot curve, consistent with the value of 3.14 eV from DFT calculations.

The PL measurements of Cs_2UCl_6 are conducted at 330 and 360 nm excitations, resulting in the emission peaks at 441 and 445 nm (Figure 4d), respectively, which was significantly different from the PL peak of CsCl in Figure S10. That means that we completely exclude the effect of CsCl luminescence. The results also indicated that PL spectrum Cs_2UCl_6 has a larger Stokes shift value compared to CsCl, which implies that U promotes more nonradiative leaps in the phototropic excitation of Cs_2UCl_6. Additionally, Cs_2UCl_6 exhibits a characteristic emission peak at 325 nm with excitation under 280 nm, indicating a vibration-coupled electron transfer. A full-width-half-maximum (fwhm) at 440−445 nm increases gradually (95 nm under 360 nm excitation, 131 nm under 330 nm excitation, and 176 nm under 280 nm excitation) as the excitation wavelength decreases. The results demonstrate the emergence of an excitation-dependent phenomenon that may be associated with the multiplet of U and the intensification of phonon scattering in the vicinity of the band as the wavelength decreases.[45,46] The reason can be attributed to the lattice vibration from the Jahn−Teller distortion of the UCl_4 unit, which strengthens electron−phonon coupling at higher excitation energies.[47] Additionally, the relaxation of hot excited states involves increased electron−phonon and phonon−phonon scattering. Changes in the density of states at higher energies further amplify the overlap of electronic wave functions and lattice vibrations. These factors collectively account for the observed excitation-energy-dependent PL behavior. The distinguishable emission peaks at 325 and 440−445 nm in Cs_2UCl_6 further indicate the presence of multiple excited states. Cs_2UCl_6 demonstrates an upward intensity trend with increasing tube voltage and X-rays, suggesting excellent X-ray energy responsiveness as shown in Figure 4e. Besides, Cs_2UCl_6 exhibits complex spectra with multiple emission peaks that emerge between 450 and 700 nm when the X-ray tube voltage increases from 20 to 50 kV, which might be related to the multiple electronic transitions in Cs_2UCl_6. The results further imply the existence of multiple excitable states in Cs_2UCl_6. The main reason for the generation of the complex multistate structure can be attributed to the high level of U−Cl hybridization according to the DOS. Therefore, the Cs_2UCl_6 single crystal demonstrates promising applications in dose−response scenarios due to its energy responsiveness regardless of its relatively low environmental stability. However, the presence of a soluble solvent leads to Cs_2UCl_6 losing PL in water. Extensive studies have demonstrated the significant advantages of MOFs in solidifying, adsorbing, and separating U-containing compounds due to their high surface area and multiple adsorption sites.[48−50] To address the issue, the synthesized Cs_2UCl_6 was subjected to further immobilization in vitrified MOFs through the hot-pressing technique, thereby enhancing its stability (Figure S11).[51,52] The as-sintered pellet exhibits a light green color with a theoretical density higher than 95%, suggesting successful consolidation of the perovskite into the MOF matrix. Optical testing has revealed a stable wavelength of 452 nm for the light emission signal of the composite material under 360 nm excitation in Figure 4f. A stable PL spectrum was obtained after water corrosion for 72 h. However, a 5 nm blue shift of the peak was observed in comparison to the spectrum before water corrosion. Additionally, new peaks at 523 and 546 nm were observed from the PL spectrum. The positions of these two peaks coincided with the luminescence peaks of uranyl.[53] The findings indicate that ZIF plays a protective role in preventing water-induced structural damage to Cs_2UCl_6 during the vitrification process. Following a period with 72 h of water corrosion and subsequent re-exposure to air, a part of U^{4+} might be oxygenated, resulting in the formation of uranyl clusters. Overall, there has been a notable enhancement in the stability of Cs_2UCl_6 in water, but the microstructure evolution mechanism in water needs to be further revealed.

As mentioned before, the phase stability under an ambient environment is critical to the potential application of the Cs_2UCl_6. The thermal stability of the Cs_2UCl_6 was characterized by in situ confocal Raman and TGA. Two distinct peaks emerged prominently at 311 and 831 cm^{-1}, with the characteristic peaks shifted toward lower angles at elevated temperatures, indicating a lattice expansion beyond 50 °C as shown in Figure 5a. The interactions between atoms weaken as well as the lattice vibration intensifies with temperature increases until the peak completely disappears at 330 °C. The results indicate that the single crystal has lost its Cs_2UCl_6 character at 330 °C via the in situ Raman spectra test, suggesting that decomposition of the surface of the single crystal occurred. A slight weight loss of 0.1% is observed at the insulation stage, which is attributed to unvolatilized hydration water in the sample based on the TGA. A linear correlation between the temperature and weight loss is observed until reaching 275 °C, which can be attributed to the thermal decomposition and evaporation of Cl. Figure 5b shows a weight loss of 2.8% between 275 and 331 °C. The thermal-induced phase change can be further evidenced by the corresponding optical image, which denotes a color change from green to white spots and black. The final weight loss of Cs_2UCl_6 after thermal treatment at 500 °C is 5.11%, with a three-stage decrease in weight loss, corresponding to three thermal decomposition stages, which can be classified as Figure 5c.

The thermal decomposition pathway of Cs_2UCl_6 was further investigated by DFT calculations, which can be summarized below in Table S4. The thermal decomposition of Cs_2UCl_6 tends to start with the splitting into CsCl and UCl_4 (reaction 1). The inherent instability of Cl in UCl_4 during the heating process facilitates the loss of an acquired electron, converting UCl_4 to the lower energy formation of UCl_3. However, the realization of the reaction requires an energy of 5.44 eV, which is much higher than the reported decomposition energy values of perovskites.[46] The lattice thermal vibration reaches the decomposition energy threshold after 275 °C, consisting of a linear rapid weight loss after reaching 275 °C, which can be attributed to the interactions between Cl and U gradually weakening until completely disappearing. After that, the CsCl should dominate total weight loss above 330 °C.[54] A reasonable conclusion is inferred from the combination of in situ Raman results and theoretical calculations, namely, that the thermal stability of Cs_2UCl_6 single crystals persists up to at least 275 °C. A potential decomposition of single crystals might occur between Cs and U−Cl at temperatures exceeding this threshold.

The DFT calculations in Table S4 show that the high humidity environment might facilitate the decomposition process, where the energy required for the reaction is only 0.25 eV and a spontaneous exothermic reaction occurs with sufficient oxygen involvement. The humidity stability of the Cs_2UCl_6 was further investigated by analyzing its decomposition trend at a humidity of not less than 85%. The schematic of the experimental setup is shown in Figure S9. Samples were taken at 0, 10, and 20 min after the introduction of water vapor, while the phase degradation behavior was further studied as shown in Figure S12. A significant decrease in the diffraction intensity of Cs_2UCl_6 can be observed postexposure under water vapor for 20 min from the comparison of Figure 5d,e. Simultaneously, it can be observed that the diffraction intensity appears to be amplified around x = 800−1500 and y = 0−800, which is associated with the enhancement of high-angle diffraction peaks in Figure 5e. In addition, the SXRD data shows that triple intensity peaks shifted toward a lower angle postexposure under water vapor for 20 min, which indicated that the lattice anisotropy of the sample contracted and the bond strengths weakened. The SXRD data in Figure 5f revealed that three new peaks at positions 6.06°, 27.39°, and 30.67° had appeared with the overall diffraction intensities of Cs_2UCl_6 reduced, which indicated the water corrosion had accomplished the generation of a new phase. Characterization of the new phase determines its composition as CsCl in Figure S13. Therefore, it is evident that the final substance resulting from both thermal and chemical decompositions is CsCl. This suggests that Cs_2UCl_6 will decompose first to produce CsCl in high-humidity corrosive environments.

■ CONCLUSIONS

The current study provides a novel technique to simultaneously recover trace uranium and functionalize it into perovskite structure Cs_2UCl_6 from the PUREX process through the electronic-reduction method. Bonding characteristics were examined using DFT calculations, and the crystal structure resembles a hexagonal structure featuring uniform elemental distribution and high crystallinity, based on transmission electron microscopy with an iDPC method. The as-synthesized single crystal Cs_2UCl_6 exhibits environmentally beneficial thermal stability higher than 275 °C in ambient air based on temperature-dependent Raman spectroscopy and thermogravimetric analysis. The SXRD indicated a decomposed trend of Cs_2UCl_6 to CsCl in high-humidity corrosive environments, which might damage the application's stability. The Cs_2UCl_6 demonstrates spectral properties revealing short-wavelength emission under 280, 330, and 360 nm, suggesting U^{4+} of Cs_2UCl_6 has substantial potential as a stable scintillator or detector material due to its diverse band improvement strategies. The current study expands the atomic-scale understanding of Cs_2UCl_6 and the possibility of functionalization, providing ideas for theoretical models and methods for chemical engineering modifications and implementing U-containing nuclear waste in a radioactive environment.

■ ASSOCIATED CONTENT

Supporting Information

The Supporting Information is available free of charge at https://pubs.acs.org/doi/10.1021/acs.inorgchem.4c04076.

Video about the crystal growth process (MP4)

Supplemental relevant experimental and computational details, PL spectra, XPS spectra, XRD patterns, and DFT calculation results (PDF)

■ AUTHOR INFORMATION

Corresponding Authors

Kun Yang − *Department of Nuclear Science & Technology, Nanjing University of Aeronautics and Astronautics, Nanjing 211106, China;* orcid.org/0000-0003-0040-3523; Email: kun.yang@nuaa.edu.cn

Xianlin Qu − *Center for Microscopy and Analysis, Nanjing University of Aeronautics and Astronautics, Nanjing 211016, China;* orcid.org/0000-0001-8316-8025; Email: xianlinqu@nuaa.edu.cn

Authors

Yibo Wang − *Department of Nuclear Science & Technology, Nanjing University of Aeronautics and Astronautics, Nanjing 211106, China*

Feida Chen − *Department of Nuclear Science & Technology, Nanjing University of Aeronautics and Astronautics, Nanjing 211106, China;* orcid.org/0000-0002-1926-8563

Yanmei He − *Department of Chemical Physics and NanoLund, Lund University, Lund 22100, Sweden;* orcid.org/0000-0002-8698-1932

Daniu Han − *Department of Nuclear Science & Technology, Nanjing University of Aeronautics and Astronautics, Nanjing 211106, China*

Xiaobin Tang − *Department of Nuclear Science & Technology, Nanjing University of Aeronautics and Astronautics, Nanjing 211106, China;* orcid.org/0000-0003-3308-0468

Complete contact information is available at: https://pubs.acs.org/10.1021/acs.inorgchem.4c04076

Author Contributions

Y.W. completed the material preparation, characterization analysis, and DFT calculations. K.Y., X.T., and X.Q. designed and directed the research. F.C. provided insights into the thinking as well as the draft revisions. Y.H. participated in the analysis of the spectroscopic properties, as well as the revisions of the draft. K.Y. supervised the project and established the final version of the paper. H.N. and Y.H. provided the analysis support. All authors contributed to the manuscript and have approved the final version of the manuscript.

Notes

The authors declare no competing financial interest.

■ ACKNOWLEDGMENTS

The author would like to acknowledge the financial support provided by the Jiangsu Nature Science Foundation (BK20230898). The Postgraduate Research & Practice Innovation Program of Jiangsu Province (Grant No. KYCX23_0368). China Postdoctoral Science Foundation (2023M731673).

■ REFERENCES

(1) Ye, Y.; Jin, J.; Chen, F.; Dionysiou, D. D.; Feng, Y.; Liang, B.; Cheng, H. Y.; Qin, Z.; Tang, X.; Li, H.; Yntema, D.; Li, C.; Chen, Y.; Wang, Y. Removal and Recovery of Aqueous U(VI) by Heterogeneous Photocatalysis: Progress and Challenges. *Chem. Eng. J.* **2022**, *450*, No. 138317.

(2) Wang, Z.; Zhou, G.; Jiang, D.; Wang, S. Recent Development of $A_2B_2O_7$ System Transparent Ceramics. *Journal of Advanced Ceramics.* **2018**, *7*, 289−306.

(3) Kumar, J. R.; Kim, J. S.; Lee, J. Y.; Yoon, H. S. A Brief Review on Solvent Extraction of Uranium from Acidic Solutions. *Sep. Purif. Rev.* **2011**, *40* (2), 77−125.

(4) Zilberman, B. Y.; Puzikov, E. A.; Ryabkov, D. V.; Makarychev-Mikhailov, M. N.; Shadrin, A. Y.; Fedorov, Y. S.; Simonenko, V. A. Development, Analysis, and Simulation of a Technological Structure for Reprocessing Irradiated Nuclear Fuel from Nuclear Power Plants by Water-Extraction Methods. *At. Energy* **2009**, *107* (5), 333−347.

(5) Darda, S. A.; Gabbar, H. A.; Damideh, V.; Aboughaly, M.; Hassen, I. A Comprehensive Review on Radioactive Waste Cycle from Generation to Disposal. *J. Radioanal. Nucl. Chem.* **2021**, *329* (1), 15−31.

(6) Liu, T.; Zhang, R.; Chen, M.; Liu, Y.; Xie, Z.; Tang, S.; Yuan, Y.; Wang, N. Vertically Aligned Polyamidoxime/Graphene Oxide Hybrid Sheets' Membrane for Ultrafast and Selective Extraction of Uranium from Seawater. *Adv. Funct. Mater.* **2022**, *32* (14), No. 2111049.

(7) Li, N.; Yang, L.; Wang, D.; Tang, C.; Deng, W.; Wang, Z. High-Capacity Amidoxime-Functionalized β-Cyclodextrin/Graphene Aerogel for Selective Uranium Capture. *Environ. Sci. Technol.* **2021**, *55* (13), 9181−9188.

(8) Hanna, S. L.; Farha, O. K. Energy-Structure-Property Relationships in Uranium Metal-Organic Frameworks. *Chem. Sci.* **2023**, *14*, 4219−4229.

(9) Cui, W.; Li, F.; Xu, R.; Zhang, C.; Chen, X.; Yan, R.; Liang, R.; Qiu, J. Regenerable Covalent Organic Frameworks for Photo-enhanced Uranium Adsorption from Seawater. *Angew. Chem.* **2020**, *132* (40), 17837−17843.

(10) Zhang, Q. Y.; Zhang, L. J.; Zhu, J. Q.; Gong, L. L.; Huang, Z. C.; Gao, F.; Wang, J. Q.; Xie, X. Q.; Luo, F. Ultra-Selective Uranium Separation by in-Situ Formation of π-f Conjugated 2D Uranium-Organic Framework. *Nat. Commun.* **2024**, *15* (1), 453.

(11) Kim, J.; Tsouris, C.; Oyola, Y.; Janke, C. J.; Mayes, R. T.; Dai, S.; Gill, G.; Kuo, L. J.; Wood, J.; Choe, K. Y.; Schneider, E.; Lindner, H. Uptake of Uranium from Seawater by Amidoxime-Based Polymeric Adsorbent: Field Experiments, Modeling, and Updated Economic Assessment. *Ind. Eng. Chem. Res.* **2014**, *53* (14), 6076−6083.

(12) Liu, T.; Li, Z.; Zhang, X.; Tan, H.; Chen, Z.; Wu, J.; Chen, J.; Qiu, H. Metal-Organic Framework-Intercalated Graphene Oxide Membranes for Selective Separation of Uranium. *Anal. Chem.* **2021**, *93* (48), 16175−16183.

(13) Szlachta, M.; Neitola, R.; Peräniemi, S.; Vepsäläinen, J. Effective Separation of Uranium from Mine Process Effluents Using Chitosan as a Recyclable Natural Adsorbent. *Sep. Purif. Technol.* **2020**, *253*, No. 117493.

(14) Wylie, E. M.; Manard, B. T.; Quarles, C. D.; Meyers, L. A.; Xu, N. An Automated Micro-Separation System for the Chromatographic Removal of Uranium Matrix for Trace Element Analysis by ICP-OES. *Talanta* **2018**, *189* (May), 24−30.

(15) Liao, J.; Xiong, T.; Ding, L.; Zhang, Y.; Zhu, W. Effective Separation of Uranium(VI) from Wastewater Using a Magnetic Carbon as a Recyclable Adsorbent. *Sep. Purif. Technol.* **2022**, *282*, No. 120140.

(16) Hu, D.; Jiang, X. Stepwise Benzylic Oxygenation via Uranyl-Photocatalysis. *Green Chem.* **2022**, *24* (1), 124−129.

(17) Zhang, S. Y.; Tang, S. B.; Jiang, Y. X.; Zhu, R. Y.; Wang, Z. X.; Long, B.; Su, J. Mechanism of the Visible-Light-Promoted C(sp^3)-H

Oxidation via Uranyl Photocatalysis. *Inorg. Chem.* **2024**, *63* (5), 2418−2430.

(18) Zhang, Y.; Wang, X.; Xu, K.; Zhai, F.; Shu, J.; Tao, Y.; Wang, J.; Jiang, L.; Yang, L.; Wang, Y.; Liu, W.; Su, J.; Chai, Z.; Wang, S. Near-Unity Energy Transfer from Uranyl to Europium in a Heterobimetallic Organic Framework with Record-Breaking Quantum Yield. *J. Am. Chem. Soc.* **2023**, *145* (24), 13161−13168.

(19) Lee, Y. H.; Atoini, Y.; Kusumoto, S.; Hayami, S.; Kim, Y.; Harrowfield, J.; Thuéry, P. High Photoluminescence Quantum Yield of a Uranyl Ion Complex with the Hemi-Zwitterion 1,3-Bis-(Carboxylatomethyl)-1H-Benzimidazol-3-Ium. *Polyhedron* **2024**, *262*, No. 117172.

(20) Zhang, M.; Liang, C.; Cheng, G. D.; Chen, J.; Wang, Y.; He, L.; Cheng, L.; Gong, S.; Zhang, D.; Li, J.; Hu, S. X.; Diwu, J.; Wu, G.; Wang, Y.; Chai, Z.; Wang, S. Intrinsic Semiconducting Behavior in a Large Mixed-Valent Uranium(V/VI) Cluster. *Angew. Chem., Int. Ed.* **2021**, *60* (18), 9886−9890.

(21) Wang, Y.; Yin, X.; Chen, J.; Wang, Y.; Chai, Z.; Wang, S. Gleaming Uranium: An Emerging Emitter for Building X-Ray Scintillators. *Chem. - Eur. J.* **2020**, *26* (9), 1900−1905.

(22) Wang, Y.; Yin, X.; Liu, W.; Xie, J.; Chen, J.; Silver, M. A.; Sheng, D.; Chen, L.; Diwu, J.; Liu, N.; Chai, Z.; Albrecht-Schmitt, T. E.; Wang, S. Emergence of Uranium as a Distinct Metal Center for Building Intrinsic X-Ray Scintillators. *Angew. Chem., Int. Ed.* **2018**, *57* (26), 7883−7887.

(23) Xie, J.; Wang, Y.; Liu, W.; Yin, X.; Chen, L.; Zou, Y.; Diwu, J.; Chai, Z.; Albrecht-Schmitt, T. E.; Liu, G.; Wang, S. Highly Sensitive Detection of Ionizing Radiations by a Photoluminescent Uranyl Organic Framework. *Angew. Chem., Int. Ed.* **2017**, *56* (26), 7500−7504.

(24) Jiao, L.; Howard, S.; Ran, S.; Wang, Z.; Rodriguez, J. O.; Sigrist, M.; Wang, Z.; Butch, N. P.; Madhavan, V. Chiral Superconductivity in Heavy-Fermion Metal UTe_2. *Nature* **2020**, *579* (7800), 523−527.

(25) Fernandes, R. M.; Coldea, A. I.; Ding, H.; Fisher, I. R.; Hirschfeld, P. J.; Kotliar, G. Iron Pnictides and Chalcogenides: A New Paradigm for Superconductivity. *Nature* **2022**, *601* (7891), 35−44.

(26) Aishwarya, A.; May-Mann, J.; Raghavan, A.; Nie, L.; Romanelli, M.; Ran, S.; Saha, S. R.; Paglione, J.; Butch, N. P.; Fradkin, E.; Madhavan, V. Magnetic-Field-Sensitive Charge Density Waves in the Superconductor UTe_2. *Nature* **2023**, *618* (7967), 928−933.

(27) O'Sullivan, S. E.; Montoya, E.; Sun, S. K.; George, J.; Kirk, C.; Dixon Wilkins, M. C.; Weck, P. F.; Kim, E.; Knight, K. S.; Hyatt, N. C. Crystal and Electronic Structures of A_2NaIO_6 Periodate Double Perovskites (A = Sr, Ca, Ba): Candidate Wasteforms for I-129 Immobilization. *Inorganic Chemistry.* **2020**, *59*, 18407−18419.

(28) Nirala, G.; Yadav, D.; Upadhyay, S. Ruddlesden-Popper Phase A_2BO_4 Oxides: Recent Studies on Structure, Electrical, Dielectric, and Optical Properties. *Journal of Advanced Ceramics.* **2020**, *9*, 129−148.

(29) Chen, L.; Li, B.; Guo, J.; Zhu, Y.; Feng, J. High-Entropy Perovskite $RETa_3O_9$ Ceramics for High-Temperature Environmental/Thermal Barrier Coatings. *Journal of Advanced Ceramics.* **2022**, *11*, 556−569.

(30) Folgueras, M. C.; Jiang, Y.; Jin, J.; Yang, P. High-Entropy Halide Perovskite Single Crystals Stabilized by Mild Chemistry. *Nature* **2023**, *621* (7978), 282−288.

(31) Yang, K.; Zhu, W.; Riley, B. J.; Vienna, J. D.; Zhao, D.; Lian, J. Perovskite-Derived Cs_2SnCl_6-Silica Composites as Advanced Waste Forms for Chloride Salt Wastes. *Environ. Sci. Technol.* **2021**, *55* (11), 7605−7614.

(32) Fedorovskiy, A. *Investigation of Lead-Free Perovskites for Optoelectronic Application*; EPFL, 2021; vol *9398*.

(33) Miner, F. J.; DeGrazio, R. P.; Byrne, J. T. Dicesium Plutonium Hexachloride, a Proposed Primary Standard for Plutonium. *Anal. Chem.* **1963**, *35* (9), 1218−1223.

(34) Gogolev, A. V.; Shilov, V. P.; Peretrukhin, V. F.; Yusov, A. B.; Fedoseev, A. M. Formation of a Sol of Mixed U(IV) • U(VI) Hydroxide in Aqueous Solutions with PH 1.5−4. *Radiochemistry* **2008**, *50* (4), 349−353.

(35) Karbowiak, M.; Karbowiak, M. Energy-Level Calculations for the $5f^26d^1$ Configuration of U^{3+} in Cs_2NaYCl_6 and $SrCl_2$ Single Crystals. In *Symmetry, Spectrosc.*; SCHUR, 2006; p 147.

(36) Zhu, W.; Shen, J.; Li, M.; Yang, K.; Bu, W.; Sun, Y. Y.; Shi, J.; Lian, J. Kinetically Controlled Growth of Sub-Millimeter 2D Cs_2SnI_6 Nanosheets at the Liquid−Liquid Interface. *Small* **2021**, *17* (4), No. 2006279.

(37) Kresse, G.; Hafner, J. Ab Initio Molecular Dynamics for Liquid Metals. *Phys. Rev. B* **1993**, *47* (1), 558−561.

(38) Kresse, G.; Furthmüller, J. Efficiency of Ab-Initio Total Energy Calculations for Metals and Semiconductors Using a Plane-Wave Basis Set. *Comput. Mater. Sci.* **1996**, *6* (1), 15−50.

(39) Wang, V.; Xu, N.; Liu, J. C.; Tang, G.; Geng, W. T. VASPKIT: A User-Friendly Interface Facilitating High-Throughput Computing and Analysis Using *VASP* Code. *Comput. Phys. Commun.* **2021**, *267*, No. 108033.

(40) El Jamal, G.; Gouder, T.; Eloirdi, R.; Jonsson, M. X-Ray and Ultraviolet Photoelectron Spectroscopy Studies of Uranium(Iv), (v) and(vi) Exposed to H_2O-Plasma under UHV Conditions. *Dalt. Trans.* **2021**, *50* (2), 729−738.

(41) Shewale, P. S.; Ung Sim, K.; Kim, Y. B.; Kim, J. H.; Moholkar, A. V.; Uplane, M. D. Structural and Photoluminescence Characterization of SnO_2: F Thin Films Deposited by Advanced Spray Pyrolysis Technique at Low Substrate Temperature. *J. Lumin.* **2013**, *139*, 113−118.

(42) Jung, M. H.; Chu, M. J. Synthesis of Hexagonal ZnO Nanodrums, Nanosheets and Nanowires by the Ionic Effect during the Growth of Hexagonal ZnO Crystals. *Journal of Materials Chemistry C* **2014**, *2*, 6675−6682.

(43) Krukau, A. V.; Vydrov, O. A.; Izmaylov, A. F.; Scuseria, G. E. Influence of the Exchange Screening Parameter on the Performance of Screened Hybrid Functionals. *J. Chem. Phys.* **2006**, *125*, 224106.

(44) Hinuma, Y.; Pizzi, G.; Kumagai, Y.; Oba, F.; Tanaka, I. Band Structure Diagram Paths Based on Crystallography. *Comput. Mater. Sci.* **2017**, *128*, 140−184.

(45) Warzecha, E.; Celis-Barros, C.; Dilbeck, T.; Hanson, K.; Albrecht-Schmitt, T. E. High-Pressure Studies of Cesium Uranyl Chloride. *Inorganic Chemistry.* **2019**, *58*, 228−233.

(46) Chen, Y.; Shi, T.; Liu, P.; Xie, W.; Chen, K.; Xu, X.; Shui, L.; Shang, C.; Chen, Z.; Yip, H. L.; Zhou, G.; Wang, X. The Distinctive Phase Stability and Defect Physics in $CsPbI_2Br$ Perovskite. *Journal of Materials Chemistry A* **2019**, *7*, 20201−20207.

(47) Halcrow, M. A. Jahn−Teller Distortions in Transition Metal Compounds, and Their Importance in Functional Molecular and Inorganic Materials. *Chem. Soc. Rev.* **2013**, *42* (4), 1784−1795.

(48) Chen, T.; Yu, K.; Dong, C.; Yuan, X.; Gong, X.; Lian, J.; Cao, X.; Li, M.; Zhou, L.; Hu, B.; He, R.; Zhu, W.; Wang, X. Advanced Photocatalysts for Uranium Extraction: Elaborate Design and Future Perspectives. *Coord. Chem. Rev.* **2022**, *467*, No. 214615.

(49) Shi, S.; Liu, J.; Shu, J.; Wu, P.; Zhao, C.; Liu, N.; Lan, T. Uranium(VI) Adsorption from Carbonate Solutions Using Cetyltrimethylammonium Bromide Modified Purified-Bentonite-MOF Composite. *Appl. Clay Sci.* **2023**, *241* (May), No. 106986.

(50) Liu, T.; Tang, S.; Wei, T.; Chen, M.; Xie, Z.; Zhang, R.; Liu, Y.; Wang, N. Defect-Engineered Metal-Organic Framework with Enhanced Photoreduction Activity toward Uranium Extraction from Seawater. *Cell Reports Phys. Sci.* **2022**, *3* (5), No. 100892.

(51) Ao, D.; Yang, Z.; Qiao, Z.; Sun, Y.; Zhang, Z.; Guiver, M. D.; Zhong, C. Metal−Organic Framework Crystal−Glass Composite Membranes with Preferential Permeation of Ethane. *Angew. Chem., Int. Ed.* **2023**, *62* (28), No. e202304535.

(52) Hou, J.; Chen, P.; Shukla, A.; Krajnc, A.; Wang, T.; Li, X.; Doasa, R.; Tizei, L. H. G.; Chan, B.; Johnstone, D. N.; Lin, R.; Schülli, T. U.; Martens, I.; Appadoo, D.; Ari, M. S.; Wang, Z.; Wei, T.; Lo, S. C.; Lu, M.; Li, S.; Namdas, E. B.; Mali, G.; Cheetham, A. K.; Collins, S. M.; Chen, V.; Wang, L.; Bennett, T. D. Liquid-Phase Sintering of Lead Halide Perovskites and Metal-Organic Framework Glasses. *Science.* **2021**, *374* (6567), 621−625.

(53) Flint, C. D.; Tanner, P. A. Luminescence Spectrum of Cs_2UO2Cl_4. *Journal of the Chemical Society, Faraday Transactions 2: Molecular and Chemical Physics* **1978**, *74*, 2210−2217.

(54) Zakir'yanova, I. D.; Arkhipov, P. A. Raman Spectra and Conductivity of $PbO-PbCl_2-CsCl$ Melts. *Russian Metallurgy (Metally).* **2017**, *2017*, 86−90.